AFRL-RX-WP-TR-2020-0146

UNDERSTANDING TEMPERATURE AND MICROSTRUCTURE EFFECTS ON DAMAGE ACCUMULATION IN TI ALLOYS UNDER SUSTAINED-PEAK LOW-CYCLE FATIGUE (SPLCF)

James Barber
University of Michigan, Department of Mechanical Engineering

08 MAY 2020
Final Report

AIR FORCE RESEARCH LABORATORY
MATERIALS AND MANUFACTURING DIRECTORATE
WRIGHT-PATTERSON AIR FORCE BASE, OH 45433-7750
AIR FORCE MATERIEL COMMAND
UNITED STATES AIR FORCE

NOTICE AND SIGNATURE PAGE

Using Government drawings, specifications, or other data included in this document for any purpose other than Government procurement does not in any way obligate the U.S. Government. The fact that the Government formulated or supplied the drawings, specifications, or other data does not license the holder or any other person or corporation; or convey any rights or permission to manufacture, use, or sell any patented invention that may relate to them.

This report is the result of contracted fundamental research deemed exempt from public affairs security and policy review in accordance with SAF/AQR memorandum dated 10 Dec 08 and AFRL/CA policy clarification memorandum dated 16 Jan 09. This report is available to the general public, including foreign nationals.

Copies may be obtained from the Defense Technical Information Center (DTIC) (http://www.dtic.mil).

AFRL-RX-WP-TR-2020-0146 HAS BEEN REVIEWED AND IS APPROVED FOR PUBLICATION IN ACCORDANCE WITH ASSIGNED DISTRIBUTION STATEMENT.

//SIGNATURE//_____	//SIGNATURE//_____
PATRICK GOLDEN	DAVID LEE
Work Unit Manager	Branch Chief
Metals Branch	Metals Branch
Structural Materials Division	Structural Materials Division
Materials and Manufacturing Directorate	Materials and Manufacturing Directorate

This report is published in the interest of scientific and technical information exchange, and its publication does not constitute the Government's approval or disapproval of its ideas or findings.

REPORT DOCUMENTATION PAGE

Form Approved
OMB No. 074-0188

1. REPORT DATE (DD-MM-YYYY)	2. REPORT TYPE	3. DATES COVERED *(From – To)*
08 May 2020	Final	15 April 2016 – 08 April 2020

4. TITLE AND SUBTITLE
UNDERSTANDING TEMPERATURE AND MICROSTRUCTURE EFFECTS ON DAMAGE ACCUMULATION IN Ti ALLOYS UNDER SUSTAINED-PEAK LOW-CYCLE FATIGUE (SPLCF)

5a. CONTRACT NUMBER
FA8650-16-C-5235

5b. GRANT NUMBER

5c. PROGRAM ELEMENT NUMBER
62102F

6. AUTHOR(S)
James Barber

5d. PROJECT NUMBER
4347

5e. TASK NUMBER

5f. WORK UNIT NUMBER
X14G

7. PERFORMING ORGANIZATION NAME(S) AND ADDRESS(ES)
University of Michigan
Department of Mechanical Engineering
2350 Hayward Street
Ann Arbor, MI 48109

8. PERFORMING ORGANIZATION REPORT NUMBER

9. SPONSORING / MONITORING AGENCY NAME(S) AND ADDRESS(ES)
Air Force Research Laboratory
Materials and Manufacturing Directorate
Wright Patterson Air Force Base, OH 45433-7750
Air Force Materiel Command
United States Air Force

10. SPONSOR/MONITOR'S ACRONYM(S)
AFRL/RXCM

11. SPONSOR/MONITOR'S REPORT NUMBER(S)
AFRL-RX-WP-TR-2020-0146

12. DISTRIBUTION / AVAILABILITY STATEMENT
DISTRIBUTION STATEMENT A. Approved for public release: distribution is unlimited..

13. SUPPLEMENTARY NOTES
Report contains color.

14. ABSTRACT ***(Maximum 200 words)***

Slip activity in dwell fatigued Ti-6Al-2Sn-4Zr-2Mo, and its relation to the microstructure, was investigated using digital image correlation and electron backscatter diffraction at room temperature, 120°C, and 200°C to span a range of dwell sensitivities. The length, orientation, and Schmid factors of the grains through which slip traces traversed, and the active slip family of each trace, were examined to identify critical grain characteristics in the percolation of long-range slip on the specimen surface. It was found that slip accumulated more rapidly and in greater amounts at temperatures that exhibit dwell sensitivity (room temperature and 120°C) versus not (200°C). At all temperatures, plasticity occurred primarily by long-range basal slip through co-located grains with a high basal Schmid factor. These findings indicate that microstructure, particularly the distribution of basally soft grains, dictates the location of slip accumulation regardless of temperature. The grains exhibiting this type of deformation were sub-features of microtextured regions defined using current methods, indicating that these approaches are not sufficient indicators of whether a microtextured region will develop long-range slip. The observed slip activity suggests the necessity of grain interconnectivity and a smaller spread in c-axes when identifying the boundaries of a microtextured region.

15. SUBJECT TERMS
Titanium, Dwell Fatigue, Microtexture, Digital Image Correlation

16. SECURITY CLASSIFICATION OF:			17. LIMITATION OF ABSTRACT	18. NUMBER OF PAGES	19a. NAME OF RESPONSIBLE PERSON *(Monitor)*
a. REPORT	b. ABSTRACT	c. THIS PAGE			Patrick Golden
Unclassified	Unclassified	Unclassified	SAR	38	19b. TELEPHONE NUBER *(include area code)* (937) 255-5438

Standard Form 298 (Rev. 2-89)
Prescribed by ANSI Std. Z39-18

TABLE OF CONTENTS

LIST OF FIGURES

Figure **Page**

LIST OF TABLES

ABSTRACT

Slip activity in dwell fatigued Ti-6Al-2Sn-4Zr-2Mo, and its relation to the microstructure, was investigated using digital image correlation and electron backscatter diffraction at room temperature, 120°C, and 200°C to span a range of dwell sensitivities. The length, orientation, and Schmid factors of the grains through which slip traces traversed, and the active slip family of each trace, were examined to identify critical grain characteristics in the percolation of long-range slip on the specimen surface. It was found that (at an equivalent fraction of yield strength) slip accumulated more rapidly and in greater amounts at temperatures that exhibit dwell sensitivity (room temperature and 120°C) versus not (200°C). At all temperatures, plasticity occurred primarily by long-range basal slip through co-located grains with a high basal Schmid factor. These findings indicate that microstructure, particularly the distribution of basally soft grains, dictates the location of slip accumulation regardless of temperature. The grains exhibiting this type of deformation were sub-features of microtextured regions defined using current methods, indicating that these approaches are not sufficient indicators of whether a microtextured region will develop long-range slip. The observed slip activity suggests the necessity of grain interconnectivity and a smaller spread in c-axes when identifying the boundaries of a microtextured region.

PREFACE

The authors gratefully acknowledge financial support from the Air Force Research Labs under Contract #FA8650-16-C-5235 and the National Science Foundation Graduate Research Fellowship under Grant No. 1256260 DGE. The authors thank Mr. Kirk Fields for help and insights with experimental methodologies and testing. The authors had informative conversations on instrumentation and experimental methodologies with Glenn Balbus, Dave Bothman, Mark Cornish, Darin Randall, Aidan Taylor, and Chris Torbet.

1. SUMMARY

The aim of this work was to examine the effects of temperature and microstructure on localized damage accumulation during sustained-peak low-cycle fatigue (SPLCF, also known as dwell fatigue) of Ti6242. Ti6242 is a widely used aerospace alloy that exhibits a substantial sensitivity to dwell fatigue, where a significant reduction in fatigue life occurs when load is held at a maximum value instead of being continuously cycled. Dwell sensitivity and load shedding depend on the local microstructure, specifically the presence of microtextured regions (MTRs) where microtexture refers to the clustering of α grains and transformed beta regions with similar crystallographic orientation. This research employed a combination of scanning electron microscopy, digital image correlation, and large data analyses techniques to examine the accumulation of microscale strain heterogeneities in relation to the underlying microstructure. An *ex-situ* study of plastic strain accumulation in Ti-6242 was conducted under dwell fatigue loading at room temperature (RT), 120°C, and 200°C to characterize slip activity and its effects on dwell fatigue lifetimes. Our findings indicate that current segmentation approaches may not be sufficient to capture the intricate details that govern whether or not a particular MTR will develop long-range slip. Rather than slip being accommodated homogeneously and diffusely throughout soft-oriented MTRs, we found that plastic slip was instead accommodated by subfeatures within classically segmented MTRs. The observed slip systems and Schmid factors in this study redefine and narrow our definition of MTRs that are damaging under dwell fatigue loading. In particular, these results suggest the necessity of grain interconnectivity and a smaller spread in c-axes should be used when identifying the boundaries of a MTR. Additionally, it was found that slip accumulated more rapidly and in greater amounts at temperatures that exhibit a dwell debit in Ti-6242 (RT and 120°C) versus that which does not (200°C), which may be related to the temperature dependence of strain rate sensitivity. At all temperatures (RT, 120°C, and 200°C), new slip traces occurred largely in regions that had already exhibited slip, supporting the conjecture that slip and its evolution under dwell cycling are microstructurally driven by cooperative grain groupings that allow the traversal of contiguous slip activity. Grains that behaved cooperatively and exhibited long-range plastic slip were (i) co-located; (ii) had high basal and/or pyramidal Schmid factors, with basally-soft slip dominating; and (iii) exhibited small variations in orientation. Deformation at all temperatures was largely accommodated by long-range basal slip in co-located grains with high basal Schmid factors, and shorter pyramidal slip in nearby grains with high pyramidal Schmid factors. No significant prismatic or pyramidal slip was observed to occur independently in areas far from those of basal slip. This is likely due to internal stresses initiating the activation of less favorable slip in the neighboring grains following the exhaustion of basal slip, indicating that the dwell debit is not solely orientation dependent and that we must also consider the effect of microstructural neighborhood.

2. INTRODUCTION

Near-alpha titanium alloys have an excellent strength-to-weight ratio, highly tailorable mechanical properties, and are corrosion resistant, leading to their widespread adoption in aerospace applications. In particular, the titanium alloy Ti-6242 is under widespread use in the compressor disks and blades of gas turbine engines. The compressor disk and blades within the intermediate pressure section of gas turbine engines are considered life critical and require reliable lifetime predictions [1]. When designing and maintaining these components, a parameter for which the mechanisms are not well understood is dwell fatigue. Due to this knowledge gap, compressor disks are failing unexpectedly early, causing dangerous and expensive failures.

Dwell fatigue is characterized by a constant hold at the peak of each load cycle, creating a trapezoidal waveform. The hold models the sustained peak stress that components experience during flight, between take-off and landing. Each flight cycle dramatically reduces the lifetime of titanium alloy turbine disks when compared to the lifetime predicted by standard cyclic fatigue loading calculations. This reduction in lifetime is termed the *dwell debit*. In Ti-6242, the dwell debit is commonly ten to twenty times below the lifetime predicted by low cycle fatigue calculations. In near-alpha titanium alloys, a phenomenon known as load shedding in alpha grain is hypothesized to be the cause of this lifetime reduction.

Load shedding stems from crystallographic anisotropy, wherein grains with crystallographic orientations favorable for deformation undergo plastic deformation, thereby forcing grains that are less favorably oriented for plastic deformation to carry a higher stress. In Ti-6242, the orientation of the c-axis of the alpha grains relative to the loading direction produces a distinct elastic modulus in each grain. Grains with their c-axis near parallel to the loading direction are termed “hard grains,” whereas grains with their c-axis near perpendicular to the loading direction are termed “soft grains.” Hard grains are well oriented for pyramidal slip, whereas soft grains are well oriented for basal, or prismatic, or basal and prismatic slip. The critical resolved shear stress (CRSS) required to activate pyramidal slip is at least three times greater than the CRSS for basal and prismatic slip [2]. This difference in CRSS implies that hard grains remain resistant to plastic deformation while dislocation slip can remain active in the soft grains. When this occurs, the interaction between the hard and soft grains can be described by a modified Stroh model [3, 4]. According to the model, macroscopically applied loads can cause slip to occur in the soft grains, where dislocations move through the soft grain until they meet the hard grain boundary. The dislocations then pile up at this hard-soft interface and create a significant stress riser. The stress relaxation of the soft grain requires the hard grain to carry a higher load, and therefore the soft grain has shed its load onto the hard grain [5, 6, 7]. This region of highly localized stress creates a favorable location for crack nucleation and faceting, limiting the lifetime of the component [5]. Local microstructure and ambient temperature have a significant effect on this load transfer and the associated component failure, but the mechanisms that underlie this behavior are still under active investigation.

The effects of microstructure are an important yet little understood parameter for dwell fatigue and associated lifetimes. Dwell sensitivity and load shedding depend on the local microstructure, specifically the presence of microtextured regions (MTRs). Microtexture refers to the clustering of α grains and transformed beta regions with similar crystallographic orientation. The key attributes of MTRs important to dwell fatigue include the volume fraction, the size, and the

orientation spread of the aligned grains. These attributes may be grouped together and collectively referred to as the "intensity" of the MTRs [8]. Microtexture is believed to assist in the formation of fatigue cracks [6, 9]. Globally, MTRs are believed to define the "effective structural unit" size implying that the interfaces between these regions is the upper bound of the slip length due to the ease of slip transmission between grains with similar orientation [9-15]. It has been postulated that load shedding is dictated by the evolution of the plastic strain within the soft grain or MTR [9]. As the size of the soft region increases, there are more potential locations for long-range slip to occur, producing a greater number of dislocations in the pileup, a stronger stress concentration at the boundary with the hard grain, and a greater load-shedding effect [6,9]. MTRs can potentially produce especially large load shedding effects due to their size, as processing can produce MTRs many orders of magnitude greater than the individual grain size [6].

The mechanisms behind load shedding have been observed to be temperature dependent. The most significant dwell debit for Ti-6242 has been observed at approximately 120°C, with dwell sensitivity essentially disappearing at temperatures above nominally 200°C [16]. However, there are different hypotheses under investigation for how this occurs. Two current theories on the role of temperature in load shedding are as follows:

1. The thermal dependence of load shedding is due to the decrease in the difference in strengths of different grain orientations with increasing temperature, as determined through Crystal Plasticity Finite Element (CPFE) modeling [17]. At 120°C, the CRSS required to activate pyramidal slip is more than two times greater than CRSS for prismatic and basal slip [18]. As the temperature rises, the CRSS required for pyramidal slip decreases to match the CRSS required for basal and prismatic slip [18]. The strength mismatch between the hard and soft grains thereby diminishes, quickly redistributing the stress and allowing dislocations to traverse through the hard grain rather than collect at the boundary. It is further hypothesized that this drop in CRSS results in a more homogeneous deformation at the microscale, but this has not been thoroughly validated [5].
2. The second model identifies the effect of the temperature dependence of strain rate sensitivity in addition to the change of slip strength as the primary mechanisms for load shedding [19, 20]. During the loading cycle, dislocations are pinned at obstacles, and time-dependent thermally activated dislocation escape allows the dislocations to continue moving through the material. At 120°C in Ti-6242, the time constant associated with the activation energy required for dislocation escape is comparable to the dwell hold time. This allows for significant load shedding to occur, since the dislocations overcome their obstacle during the dwell period which allows more dislocations to nucleate and form extended pile up structures at the hard-soft boundary. At 200°C, the pinned dislocations escape so rapidly prior to the stress hold that the material reaches an equilibrium state before the dwell period, and no load shedding occurs. If the temperature is too low or the activation energy too high relative to the hold time, an additional case is proposed where load shedding is absent as the dislocations are completely unable to escape their obstacles [20, 21]. It is further shown that this strain rate sensitivity also depends upon crystallographic orientation, wherein the sensitivities of the basal and prismatic slip

systems were shown to be very different in Ti-6242 through single crystal pillar compression experiments and micro-tensile experiments [20-22]

The exact mechanisms behind load shedding and the associated dwell debit have yet to be fully understood or rigorously tested. The second model fundamentally deviates from the first, as it accounts for a thermally activated obstacle escape in addition to the temperature dependence of the material anisotropy. Both models predict a temperature dependent accumulation and redistribution of stress and strain in individual grains and MTRs during each dwell load cycle, a thermal phenomenon that has yet to be experimentally observed. Macroscopic experiments indicate that global plastic strain accumulates quickly in the first few cycles, and significant global plastic strain accumulates during the dwell hold [6.23]. Qualitative experimental work at room temperature using digital image correlation and electron speckle pattern interferometry suggests that there can be localized areas of high plastic strain within the first few cycles during dwell loading [3,24]. However, there is currently a lack of characterization to examine the impact of microstructure and dwell cycling on this localized strain accumulation, which is needed to understand the mechanisms driving load shedding and the associated dwell debit.

The work presented here characterizes the accumulation of microscale plastic strain across mm-scale field of views for Ti-6242 under dwell fatigue loading at room temperature, 120°C, and 200°C. The evolution of plastic strain and slip activity across multiple grains over each dwell cycle was investigated using a combination of electron backscatter diffraction (EBSD), scanning electron microscopy (SEM), and digital image correlation (DIC). Critical factors that allow for slip transmission were identified by examination of local strain information over several grains. The development of plastic strain accumulation with cycling was studied by comparing the slip activity of early versus later loading cycles. Grain orientation and slip family types were identified for each slip trace to understand the critical microstructural features that contribute to large regions of localized plasticity, which can result in load shedding and contribute to early crack nucleation. This information will serve to validate and inform the mechanistic understanding of load shedding and the dwell debit.

3. METHODS, ASSUMPTIONS, AND PROCEDURES

Forged and hot-rolled Ti-6242 plates of ~11.5 mm thickness provided by AFRL were processed to produce large MTRs on the order of 1-3 mm. 50mm x 50mm x 50mm plates were cut from a beta annealed billet and hot rolled at 1500°F at 10% reduction in thickness per pass to a total reduction of approximately 75% reduction. The final reduced plates were heat treated at 1750°F for 2 hours and furnace cooled. Fatigue specimens were electro discharge machined from the plates into flat pin loaded dogbone-shaped samples with dimensions of 50mm x 10mm x 1mm, with a gauge cross section of 1mm x 3mm and length of 6mm. Three samples were then mechanically ground at 240, 400, 600, and 800 grit with a final polishing to a mirror finish using a 1:4 30% hydrogen peroxide solution: MasterMet 2 Colloidal mixture. A 4 mm x 2.5 mm area of interest was defined in the center of each sample gage by placing 15 µm x 7 µm and 500 nm thick fiducial markers by platinum vapor deposition at the four corners of the region. Electron backscatter diffraction (EBSD) maps were collected over the region of interest for each sample with a step size of 2 µm per pixel using an EDAX/TSL Hikari EBSD camera. The inverse pole figure map relative to the future loading direction of each sample is shown in Figure 1.

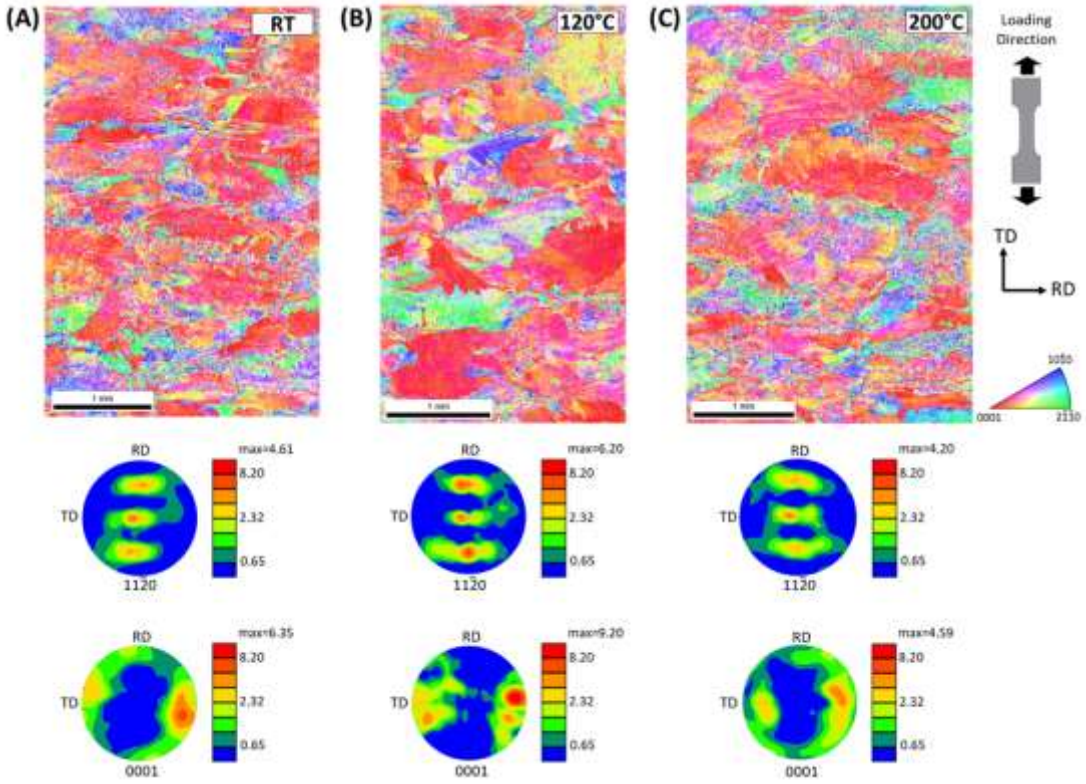

Figure 1. (Top) EBSD data and (Bottom) pole figures showing large MTRs on the length scale of 1-3mm and a moderate 0001 texture relative to the loading direction for (A) Sample A (RT), (B) Sample B (120°C), and (C) Sample C (200°C).

After EBSD, a random speckle pattern was applied to the specimen surface for SEM-DIC, in which Digital Image Correlation (DIC) is performed inside a scanning electron microscope (SEM) to characterize full-field microscale surface deformations. DIC is a full-field, length scale

independent, surface displacement measurement technique. As the specimen undergoes deformation, images are taken of the surface, and the relative displacements of the random speckle pattern features are used to calculate a full-field surface displacement map, from which the surface strains can be calculated. High resolution images were captured in-SEM and stitched together to investigate strain localization and deformation at the microstructural length scale across mm-scale fields of view [25-27]; for example, Specimen A in Table I had a 4 mm x 2.5mm field of view collected by stitching a 14 x 22 array of individual 250 µm x 250 µm SEM images. An external scan control of the electron beam was implemented to minimize the spatial and temporal image distortions that can result from ratcheting of the electron beam during SEM image collection [28, 29]. The random speckle pattern was applied following the method of Montgomery et al. [30], in which the specimen surface was sputtered with a 3 nm passivating layer of titanium followed by a 17 nm thick layer of silver in a sputter deposition system (AJA ATC 1800) equipped with 2-inch diameter sputter sources. Each sample was subsequently soaked for ~1.75 hour in a solution of 1 wt. % NaCl in distilled water to reconfigure the silver layer into a pattern of approximately 200 nm speckles. The imaging and testing parameters of each specimen are shown in Table I.

Table 1. Test Temperature, Loading and Image Conditions for Each Sample

	Test Temperature	Macroscopic Yield Strength	Tile Size	Number of Tiles	Total Imaged Area
Sample A	Room Temperature	905 MPa	300 µm	18 x 11 tiles	4 mm x 2.5 mm
Sample B	120°C	736 MPa	250µm	22x14 tiles	4 mm x 2.5 mm
Sample C	200°C	647 MPa	250µm	22 x 14 tiles	4 mm x 2.5 mm

Mechanical testing was performed at room temperature (RT), 120°C, and 200°C, as shown in Table I. These temperatures were selected to represent the following cases: (1) a dwell sensitive temperature (RT); (2) the largest dwell debit typically observed in industry (120°C); and (c) no dwell debit typically observed (200°C) [16,19]. Dwell fatigue loading is defined by a trapezoidal waveform with a 120 second load hold at the 90% of macroscopic yield with a one second load/unload. The yield strength at each of these three temperatures was determined by performing displacement-controlled uniaxial tension tests to failure in an 810 MTS test machine. The samples were pin loaded and heated using two 500 Watt induction heaters (Tempco model CRR30015), and the temperature was monitored and maintained to ±2°C with a glass fiber ratio pyrometer (model Micro-Epsilon CTRM series) and a PID controller (model Omega CN8200 series). Three tensile tests were performed at each temperature, and the 0.2% offset yield strength was averaged over these tests to determine the macroscopic yield strength of the bulk material. The macroscopic yield strengths at RT, 120°C, and 200°C were 905 MPa, 736 MPa and 647 MPa, respectively.

Load-controlled dwell fatigue experiments were performed to over 200 dwell cycles with the experimental setup shown in Figure 2. The peak load was held for 120 seconds at 90% of the macroscopic bulk yield strength. Loading was interrupted after 1, 2, 5, 50, 100, and 200 dwell cycles to collect SEM images for *ex-situ* SEM-DIC. At each imaging point, the sample was fully unloaded, cooled to room temperature in ambient air, and transferred to a SEM (FEI Teneo). After imaging, the sample was returned to the load frame, heated (if not a room temperature

test), and cycled to the next imaging point. Note that during image collection of cycle 1 for the RT condition, a beam aberration occurred and distorted a portion of the image tiles. As negligible additional strain or slip activity accumulated between cycles 1 and 2 across all temperatures, cycle 2 is used as the early cycle for comparison rather than cycle 1.

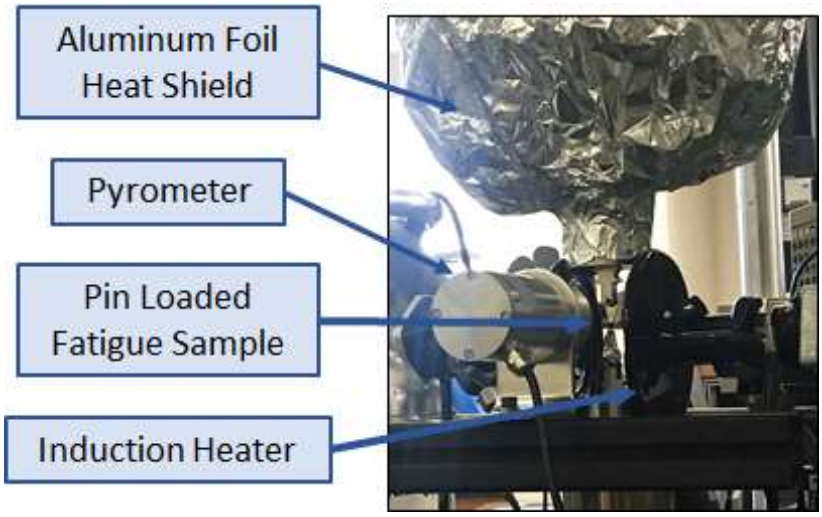

Figure 2. Experimental setup in MTS load frame for loading, specimen heating, and thermal monitoring.

The images collected during fatigue interruptions were individually correlated with commercial DIC software (VIC-2D 6) [31] to calculate displacement fields. The displacement fields were then stitched together using the method of Chen et al. [32], from which plastic strain maps over the ~4 mm x 2.5 mm region of interest were calculated. The resulting ε_{xx} ε_{yy} ε_{xy} strain maps consisted of over 300 million data points at each load step. The stitched DIC strain maps and the EBSD orientation maps were then aligned using the platinum fiducial markers and a projective transformation; although this scheme can cause alignment perturbations local to the grain boundaries that need adjustment at higher resolution studies, this alignment was sufficient at the length scale examined here [32]. The resultant strain maps exhibited long-range plastic slip features, regions of cross slip and pile up, and regions with little plastic strain, as shown in Figure 3. The patchwork background of the 200°C DIC strain maps is due to small slip activity and localized and global strains, which resulted in noisier strain fields and a much lower signal-to-noise ratio. At 200°C, the strains are so small that the background strains vary within this noise threshold, creating a tiled look. In this work, the size, shape, and location of the slip features in the strain field were analyzed to understand the effect of temperature and microstructure on residual plastic strain during dwell fatigue. The slip traces are beyond that noise threshold and were therefore able to be individually identified in the strain fields. Note that the commercial DIC algorithm used in this work is a local approach that incurs error in calculating discontinuous strains, such as those exhibited by slip activity; however, the strain values at the slip traces were not considered, but rather their presence and activity.

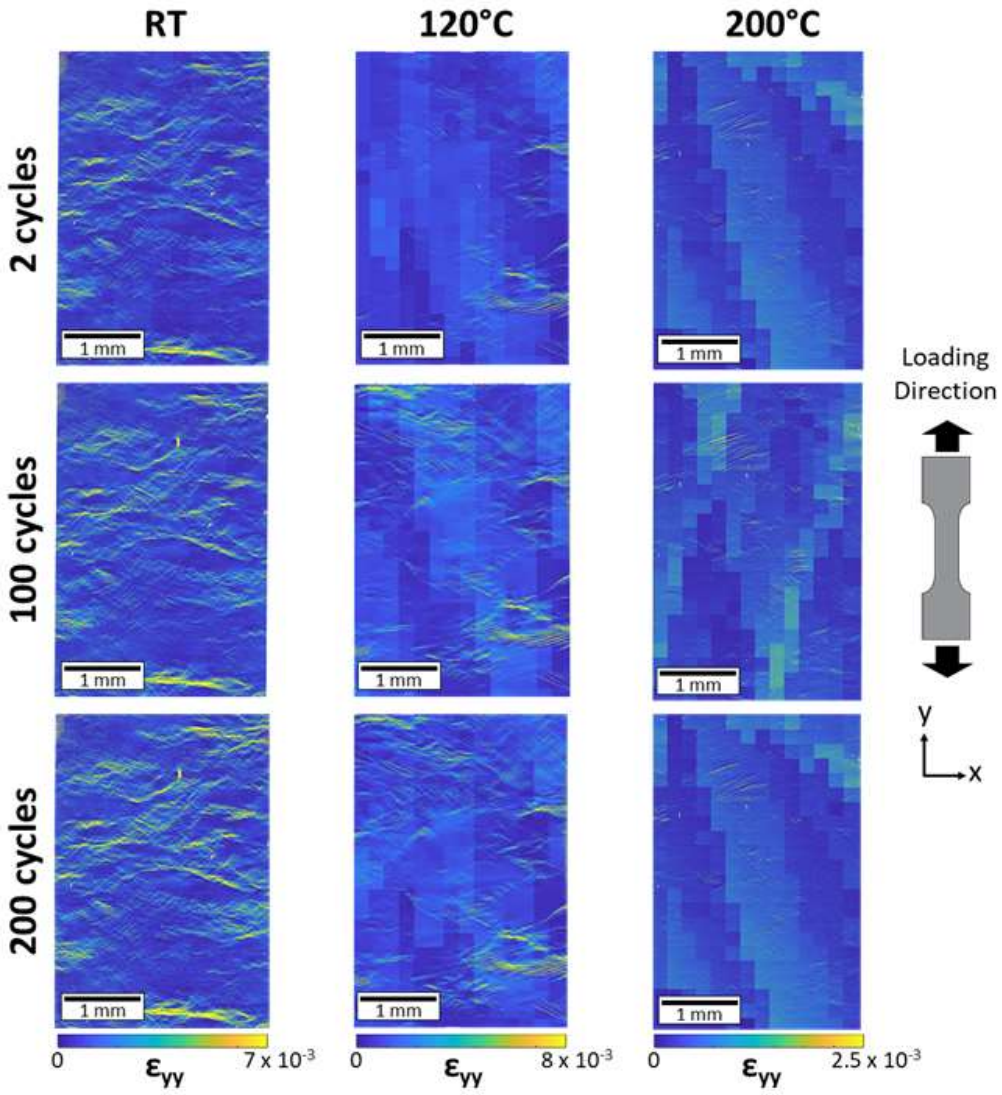

Figure 3. Axial Strain Maps for RT, 120°C, and 200°C after cycles 2, 100, and 200. There is significantly more slip activity and global strain at RT and 120°C. Note that 120°C and 200°C have background noise differences in each tile due to their low strains and low SNR. However, this work investigates the presence and activity of slip rather than the strain values, and these small differences in background noise do not impede the ability to discern slip localization.

3.1 Slip Band Segmentation Algorithm

Manual segmentation of the full datasets was infeasible due to their large size and would greatly limit the amount of data that can be analyzed. In a broader sense, as the amount of data that can be experimentally collected continues to grow rapidly, whether by SEM-DIC or by other methods such as diffraction, there is a corresponding need to increase the throughput rate of data segmentation and analysis by automated methods.

A segmentation approach for an automated first pass, followed by a refining pass on a significantly smaller subset, was created to produce binary masks of slip features through the use of clustering and image processing techniques as follows: First, each strain tile was clustered in the ε_{xx}, ε_{yy}, ε_{xy} strain components using k-means clustering, as slip traces exhibit distinctive surface strains [33]. Typically, six clusters were selected, but increased image noise caused by variations in pattern density or localized clumping required that the number of clusters be increased for a number of tiles after visual inspection. An example of a clustered tile is shown in Figure 4B. The cluster with the highest strain values encompassed the slip traces; therefore this cluster was individually plotted and subsequently converted to a binary skeletonized image. Connected component analysis was applied to identify each feature using the *bwconncomp* function in the MATLAB Image Processing Toolbox with connectivity defined through four nearest neighbors, which takes a binary image and groups regions with adjacent true pixels into distinct features. Individual long-range slip features should exist as a continuous line along a similar slope, but the skeletonization process of thick adjacent slip traces left perpendicular connected branches and loops as artifacts. To eliminate these, these loops were filled and the features re-skeletonized. Next, the feature slope was calculated by applying a linear regression to all points in the feature, Figure 4D. The branch points in the feature were identified with the image processing toolbox and removed to break the feature up into individual line segments, Figure 4F. The slopes of the individual linear subfeatures were calculated and compared to the slope of the original feature. Subfeatures with slopes perpendicular to that of the original feature were removed, and subfeatures with slopes similar to that of the original feature were reconnected by replacement of the removed branch points. This process was repeated for each individual feature from the original binarization to remove the perpendicular connections of every feature. Connected component analysis was then applied to the binary image to identify the new final linear slip traces, Figure 4H. This process was repeated for every tile in the stitched SEM-DIC strain map.

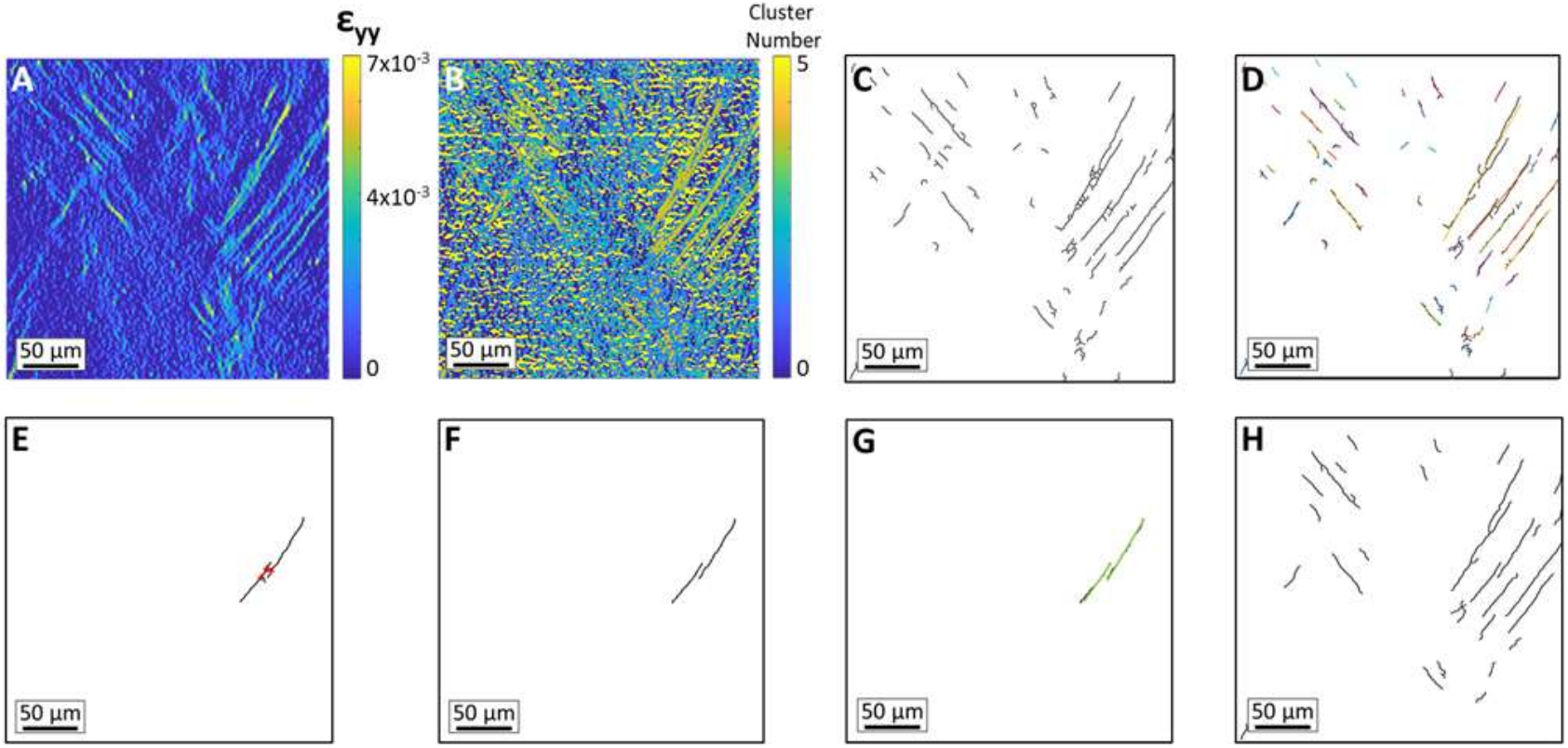

Figure 4. Slip Trace Segmentation Process: (A) Strain map of individual tile to segment slip Bands From (B) Clustered map of ε_{xx}, ε_{yy}, ε_{xy} strain components of strain tile (C) Binarized image of cluster from B with the highest strain value (D) General slope of binarized features calculated by linear regression (E) Highlighted branch points of an individual slip trace (F) Near perpendicular branches feature removed and remaining near parallel branches divided into individual features (G) Hough transform used to identify individual slopes of slip traces (H) Resultant segmentation mask of slip traces in tile A.

The slip trace segmentation was compared to the strain field for verification. Tiles that exhibited areas of higher noise, due to isolated local issues such as a pattern clump, were more difficult for the automated segmentation process to analyze. A significant amount of cross slip or pile up could also cause segmentation error in the automated technique. However, the point of this initial automated algorithm was not to create a perfect segmentation, but rather to make this process feasible in the first place by automating the majority of the segmentation, combined with a short manual segmentation step on a few select areas. During manual segmentation, the visualization of the clustered strain field aids in separating actual strain features from noise in low SNR DIC strain fields, such as the fully unloaded plastic strain fields in this study. This procedure is best suited for strain fields with a high SNR and a limited amount of cross slip. Towards the goal of a fully automated segmentation, this process could be improved with the application of machine learning techniques, such as convolutional neural networks, to increase robustness to noisy strain fields and to aid in identifying and separating intersecting slip features. Following this process, the segmentation masks were then overlaid on the strain data and stitched to produce a continuous binary segmentation mask over the entirety of the region of interest, Figure 5.

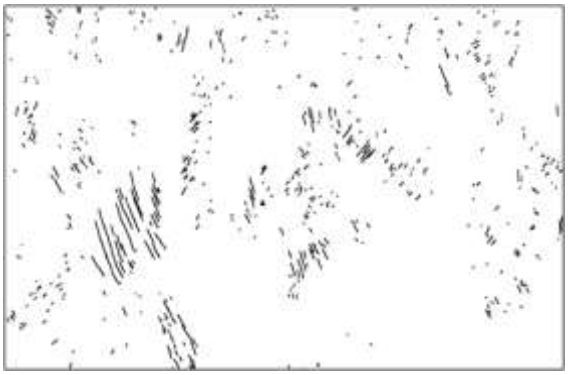

Figure 5. Full-field stitched continuous slip trace segmentation map for Sample C (200°C)

The EBSD orientation information corresponding to each plastic slip feature was indexed and extracted from the multimodal dataset of the aligned DIC strain fields, segmentation masks, and EBSD orientation maps. The Euler angles for all grains that a slip trace passed through were identified, and the statistics of the crystallographic orientations and Schmid factors among these grains were calculated. Additionally, the highest frequency grain orientation (the mode) that the individual slip trace passed through was identified as the dominant orientation using the MTEX toolbox [34]. The length of each slip trace was also calculated by using the MATLAB image processing toolbox. The length of each slip trace was measured directly from the DIC-calculated axial (ε_{xx}) strain fields, and the number of grains that each slip trace traversed was approximated using the average grain diameter. The groups of grains that work cooperatively to allow for slip at each temperature were characterized by considering the relationships between the active slip systems, grain orientations, and geometry of the surface traces. The results and implications of these analyses are presented in the results and discussion sections.

4. RESULTS AND DISCUSSION

The effects of microstructure and temperature on the presence of slip through multiple grains, and the contribution of this slip to the dwell debit of a heavily microtextured near-alpha titanium alloy, were investigated. Plastic slip activity was analyzed in Ti-6242 samples subjected to dwell fatigue at room temperature (RT), 120°C, and 200°C, Figure 3. Slip activity was compared after 2 and 200 dwell cycles following 120 second dwells at 90% of the macroscopic 0.02 percent yield strength at each temperature.

Due to the non-monotonic dwell sensitivity of Ti-6242, which increases from RT to 120°C and subsequently decreases and effectively disappears beyond 200°C, it is hypothesized that a thermodynamically driven difference in slip activity exists [5, 16, 17, 19, 20]. There is a large disparity in CRSS at low temperature that diminishes at elevated temperature. Consequently, it is tempting to conclude that slip may localize to soft MTRs at low temperature, resulting in the formation of pileups, load-shedding, and crack nucleation, while at elevated temperature more extensive slip in MTRs of all orientations eliminates the possibility of load shedding. However, our experimental findings demonstrate that this is not the case. Plastic slip traces traversing over 100 grain diameters existed at all test temperatures. In all cases, these large slip bands formed only in a contiguous collection of grains well-oriented for basal slip that were themselves embedded inside an aggregate of slightly harder grains.

There have been few attempts to quantitatively characterize microtexture. One notable exception is the work of Woodfield et al. [35, 36], who segmented MTRs from EBSD data using a 20° misorientation angle between adjacent pixels. The authors developed a regression model that related characteristics of MTRs and the primary alpha grains to dwell fatigue capability. The terms in the model included the volume fraction and size of MTRs (called the *primary alpha colony fraction* in the original paper) as well as the size and volume fraction of and degree of crystallographic alignment of the individual primary alpha particles within the MTRs. These results were used to predict fatigue lifetime as a function of microstructure for a wide range of thermomechanical processes [35]. A later formulation by Pilchak et al. [37] extended this method to group grains based on c-axis misorientation and also permitted grouping of non-contiguous pixels into MTRs. The size and shapes of the MTRs obtained by these segmentation algorithms agree well with the size and shapes of the faceted initiation sites on fracture surfaces of failed dwell fatigue specimens [7, 38].

Such observations support the hypothesis that MTRs can behave as large aggregates that allow slip bands to develop across their entirety [7,9-13], but there have only been a limited number of experiments that directly characterize this behavior [14,15]. These prior works showed the formation of slip traces through similarly oriented grains in a MTR for the first time in Ti-6-4 [14], and highlighted the importance of the physical location and orientation of the MTR relative to the loading direction [15]. Echlin et al. [14] used in-SEM DIC to map slip activity over a range of applied strains below macroscopic yield in Ti-6-4 during uniaxial tensile testing. They investigated slip band formation that occurred in soft regions of a 500 μm x 500 μm FOV encompassing a sandwich-type structure of 3-4 MTR interfaces. The material under study had a basal/transverse texture and was loaded along the rolling direction, and hence did not contain MTRs well oriented for basal slip. There were, however, individual grains well oriented for basal slip within the hard MTRs and also in more randomly oriented regions of material. It was in

these grains that basal slip was first observed after an axial strain of 0.65%. Significant amounts of prismatic slip occurred with additional loading. In some cases, these bands traversed the entirety of prismatically soft MTRs. Lunt et al. [15]. Investigated Ti-6-4 that was unidirectionally rolled to produce a strongly microtextured material. Samples were loaded in tension to 2.5% global strain, and shear strain localized in MTRs that were preferentially oriented for prismatic and basal slip activity when the MTR was physically oriented 45 and 90 degrees to the loading direction. These experiments were not at sufficient spatial resolution to identify plastic slip, but instead were targeted to capture heterogeneous strain behavior across MTRs spanning a large number of grains.

Our experimental findings suggest that current segmentation approaches may not be sufficient to capture the intricate details that govern whether or not a particular MTR will develop slip. Rather than slip being accommodated homogeneously and diffusely throughout soft-oriented MTRs, we found that plastic slip was instead accommodated by subfeatures within classically segmented MTRs, Figures 7 and 8. These subfeatures were well-oriented for basal slip and spatially arranged in a way that aligned the basal slip traces of the individual alpha particles.

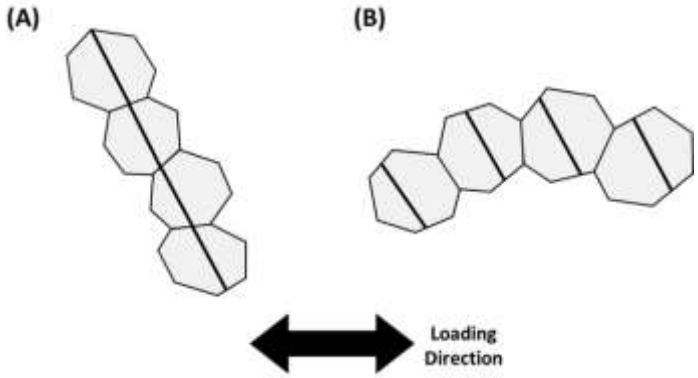

Figure 6. Co-located grains must be spatially arranged such that the basal planes of each grain align well for slip transfer. The basal slip planes of the grains in (A) are spatially arranged such that basal slip is able to transfer between grains and form slip features. While the grains in (B) are also spatially co-located and the basal places are at the same angle in each grain, the basal planes of the grains are not arranged to allow for easy basal slip transfer and therefore impede slip.

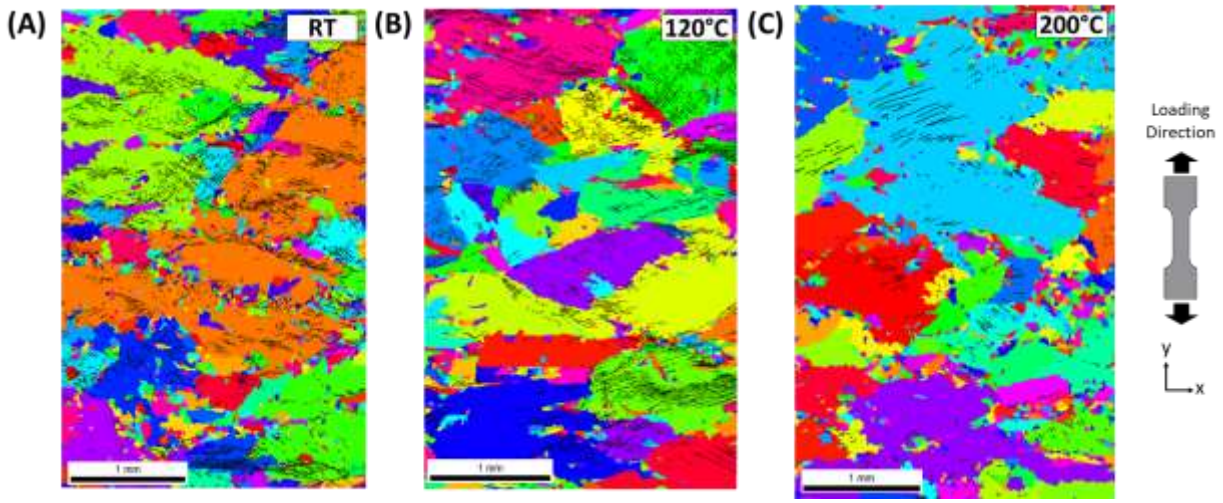

Figure 7. A traditional MTR segmentation produced by DREAM3D [39] using a 20° misorientation angle between adjacent pixels overlaid with a slip band segmentation mask obtained from DIC. Different colors represent different MTRs. Long range slip traces exist within MTRs, but they do not traverse across the entire MTR.

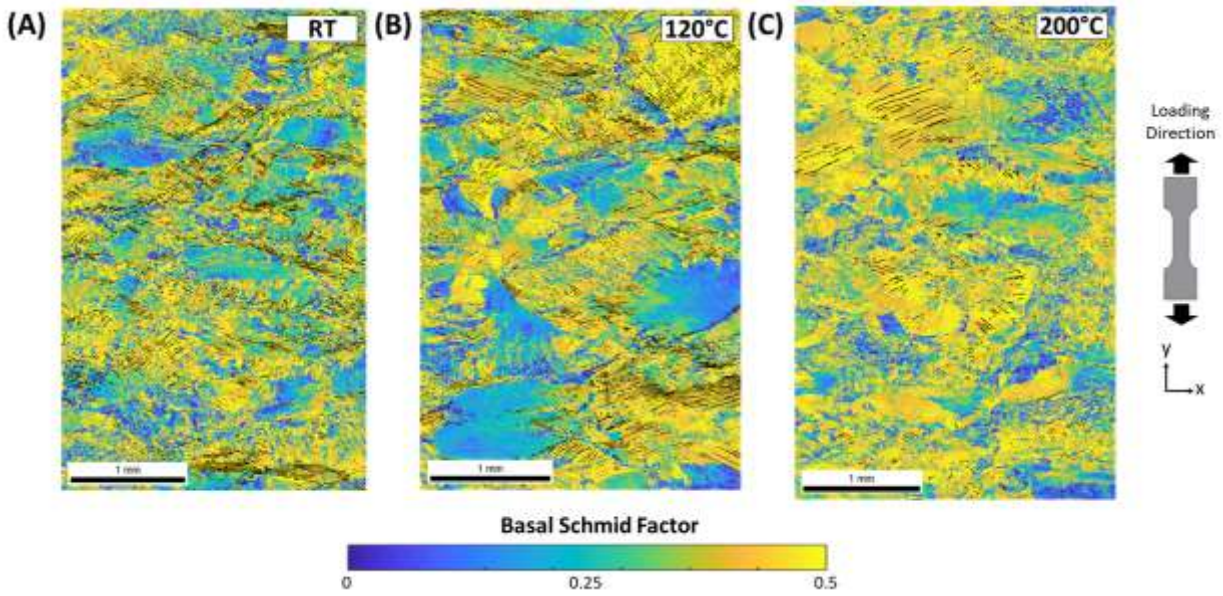

Figure 8. A color map of the basal Schmid factor for each point in the EBSD map with slip traces overlaid in black. Rather than slip traces extending through the entirety of the MTRs defined by a misorientation tolerance (Figure 7), slip occurs within and extends through regions with a high basal Schmid factor.

4.1 Number and Accumulation of Slip Traces with Dwell Cycling

At all dwell cycles, the number of slip traces at RT and 120°C was significantly larger than at 200°C (Table 2). The lack of slip activity at 200°C may be related to the temperature dependence of strain rate sensitivity [17, 19, 20] where a more rapid stress relaxation occurs with increasing temperature; this reduces the number of dislocations in a given pileup and results in lower effective stresses, due to decreased localized plastic strain accumulation. For example, after two cycles at RT and 120°C, 1909 and 2119 slip traces respectively had formed, versus only 468 slip traces at 200°C. This observation contrasts with Crystal Plasticity Finite Element (CPFE) modeling by Zhang et al. on Ti-6Al [19], a material commonly used as a model material system for Ti-6-4 and Ti6242, loaded to 95% of the temperature-corrected 0.2% offset macroscopic yield strength. Their modeling predicted a higher amount of total (elastic and plastic) strain after one cycle at 200°C than at RT and 120°C.

However, our experimental results on strain accumulation aligned with findings in CPFE modeling performed by Zhang et al. [19] and by Ozturk et al. (on textured Ti-62642) [17], although they attribute this result to different mechanisms. Both found that dwell cycling at RT and 120°C accumulate significant plastic strain after the first cycle, whereas cycling at 200°C does not. In this work, between 2 to 200 cycles, the number of slip traces increased by a factor of 2-3x at both RT and 120°C, but only increased by a factor of 1.4x at 200°C (Table II). Ozturk et al. attributed this lower strain accumulation to load shedding stemming from a reduction in plastic anisotropy at 200°C in the HCP structure of the alpha titanium grains, where the ratio of CRSS required for basal to <c+a> pyramidal slip reduces from 1.8 at RT to 1.2 at 326°C. In addition to a reduced plastic anisotropy, Zhang et al. postulated an additional effect of *cyclic load shedding* active at temperatures below ~200°C. This phenomenon implies the progressive, cycle-by-cycle redistribution of stress from the soft to the hard grain, which occurs by soft grain ratcheting of plastic strain. This occurs only during the hold at peak stress, during which creep strain accumulates via dislocation glide. The magnitude of accumulated strain is a function of the temperature-dependent strain rate sensitivity of the material. Plastic strain accumulates more readily at the intermediate temperature of 160°C when compared to RT, which may explain the increased dwell sensitivity. On the other hand, the creep rate is so high at temperatures above 230°C that strain accumulates over the order of seconds, saturates, and redistributes readily. As a result, the progressive load shedding mechanism that precedes early dwell fatigue crack nucleation is effectively shut off.

Table 2. Number of slip traces in each sample after 2 and 200 cycles, at room temperature (RT), 120°C, and 200°C.

	RT	120°C	200°C
Number of Traces After 2 Dwell Cycles	1909	2119	468
Number of Traces After 200 Dwell Cycles	6031	5685	641

At all temperatures, new slip traces occurred largely in regions that had already exhibited slip, as shown in the full-field strain maps of Figure 3. There were no locations that exhibited little slip activity after two dwell cycles and subsequently accumulated significant slip. This supports the conjecture that slip and its evolution under dwell cycling are microstructurally driven by groups of grains that allow the traversal of contiguous slip activity.

4.2 Slip Features

Of the slip features that developed after two dwell cycles, a larger percentage were long-range at 120°C and 200°C than at RT. This phenomenon is related to active slip family and grain co-location, and it is discussed in the next section. As shown in the histograms of slip lengths in Figure 9, the majority of slip traces formed at 120°C and 200°C after two dwell cycles were greater than 50 microns long (70% and 55%, respectively), versus less than 20% at RT. Additionally, ~30% of the slip traces at 120°C and 200°C were longer than 100 microns, versus only 3% of traces at RT. The distributions at 120°C and 200°C also had much longer tails, indicating that 10% of traces were longer than 200 microns (i.e. traveling through approximately 20 grains or more), with a few extreme cases where traces extended through 1000 microns (~100 grains). In contrast, at RT over 99.9% of the slip trace lengths were under 140 microns long.

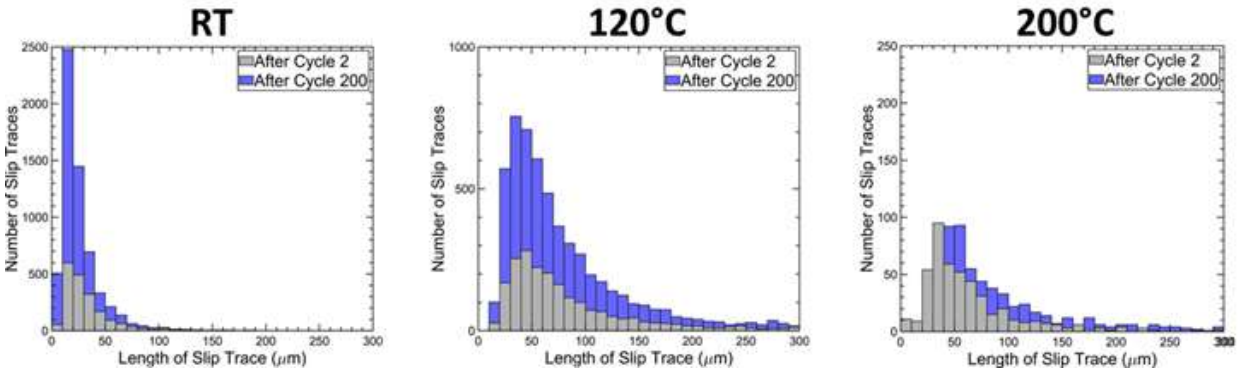

Figure 9. Distribution of Slip Feature Lengths. The y-axis varies with temperature for clarity. As shown in (A) and in Table II, significantly more slip traces formed at RT and 120°C than at 200°C. Cumulative distribution plots were also assessed to examine the tails of the distributions, but no significant differences were found.

The slip trace length distributions remained consistent with cycling at all temperatures, Figure 9. However, these distributions shifted horizontally with cycling at RT and 200°C. At RT, the distribution shifted slightly left toward shorter slip traces, indicating that most new traces were under 20 microns (<2 grains) long. At 120°C, there was little evolution in the distribution of the slip trace lengths with cycling, indicating that the lengths and regions of slip were determined from the earliest cycles. In contrast, at 200°C a shift right toward longer slip traces occurred with cycling. This shift right indicates that most of the new slip traces that formed in the 200°C case were long, with 60% of them longer than 70 microns and 10% longer than 200 microns. It is important to note that the number of slip traces at 200°C was 10% that of RT, and therefore the weight of each slip trace length contributed more significantly to the slip length distribution.

4.3 Grain Orientation Effects

At all temperatures, grains that behaved cooperatively and exhibited plastic slip were (i) co-located; (ii) had high basal and/or pyramidal Schmid factors, with basally-soft slip dominating; and (iii) exhibited small variations in orientation. These factors provided routes for easy slip percolation in basally soft regions at stresses below macroscopic yield.

For each slip feature, the dominant crystal orientation was calculated as the statistical mode of the grain orientations that the trace traversed. This dominant orientation was then used to calculate the Schmid factors for each possible slip system for that crystallographic orientation. The dominant orientation and known global stress state of the sample were also used to identify the active slip system for each of the slip traces. The slope of the projection of each slip trace on the surface of the sample was compared to the slope of the observed plastic slip surface trace. The slope of the observed surface trace was identified in the slip trace segmentation mask using a Hough transform. Only slip traces within nine degrees of the predicted slip trace were considered identifiable. Approximately 18% of traces were not able to be identified because the deviation between the measured slip band and the nearest slip plane trace exceeded the tolerance angle. The statistics of unidentified bands were investigated and there was no evidence that would indicate disproportionate misidentification of any particular slip family. The dominant crystal orientation of each slip trace is shown on an inverse pole figure (IPF) in Figure 10. For every temperature, slip traces tended to occur through grains with their c-axis near 30°-45° to the loading direction and with a high resolved shear stress on the basal plane.

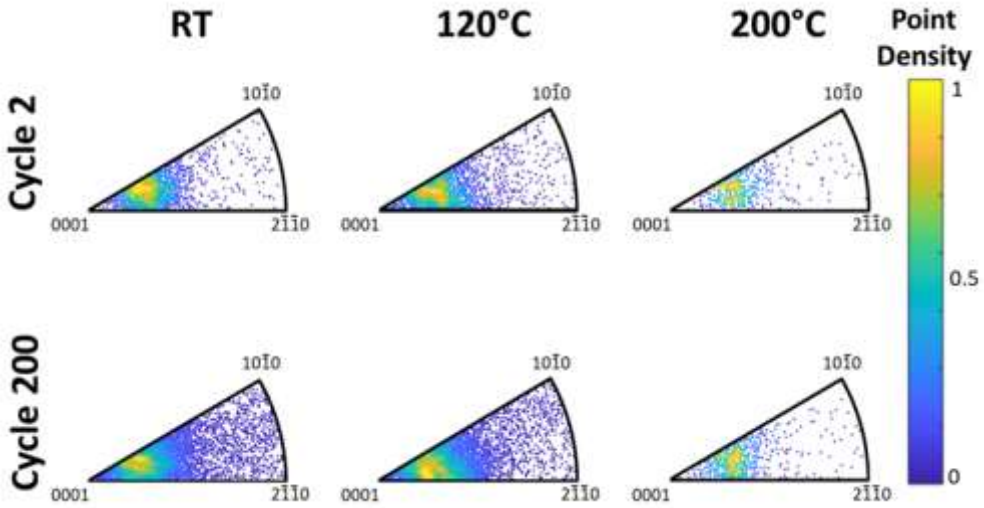

Figure 10. Slip trace orientations plotted on an IPF for samples tested at RT, 120°C, and 200°C, after 2 and 200 cycles. At all temperatures, slip traces tended to occur through grains with a high resolved shear stress on the basal plane.

At all temperatures, slip primarily occurred through grains with high basal and/or pyramidal Schmid factors, with basal slip dominating as a result of its lower CRSS. The relatively high amount of pyramidal slip was likely due to two reasons: 1) slip primarily occurred through grains with their c-axis 30-45° relative to the loading direction, and therefore had appreciable resolved shear stress on basal <a> and pyramidal <c+a> slip systems; and 2) some pyramidal slip occurred in grains with an <a> or <c+a> pyramidal Schmid factor of >0.3 (FIGURE), that were located near basal slip activity, attributed to internal stress accommodation. Schmid factors for the dominant crystal orientations were calculated for each of the 24 slip plane-direction combinations. The basal, prismatic, and pyramidal Schmid factors for each trace are reported in Figure 11 relative to slip type. At RT and 120°C, over 80% of traces had a basal Schmid factor of 0.35 or greater (at all cycles). At 200°C, over 90% of the slip traces had a basal Schmid factor of 0.35 or greater (at all cycles). Slip also required a pyramidal Schmid factor greater than 0.3, for 99.9% of slip traces and at all temperatures, Figure 11.

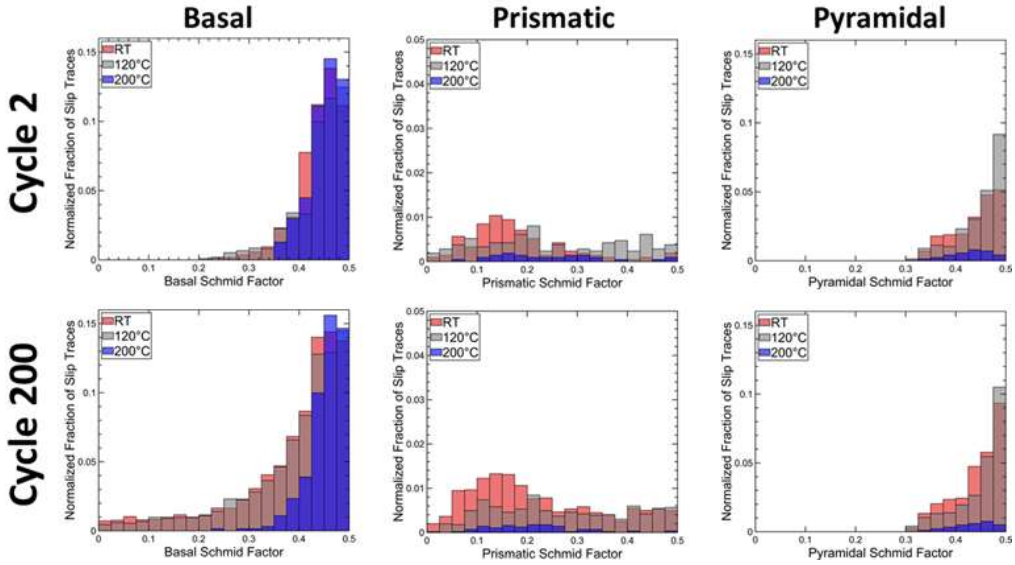

Figure 11. Histogram of the (A) Basal, (B) Prismatic, (C) Pyramidal Schmid factors of each slip trace at RT, 120°C, 200°C. At all temperatures, slip primarily occurred through grains with high basal and pyramidal Schmid factors. In the case of prismatic slip, the small number of traces affected the distribution shape (note the y-axis is correspondingly set to 5% in this plot for visualization).

The grains that each slip trace traversed exhibited small orientation variations. The standard deviation of the basal Schmid factor for the grains traversed by each slip trace was less than 0.25, Figure 12. For each slip trace, the basal Schmid factor was calculated for each grain that the trace passed through.

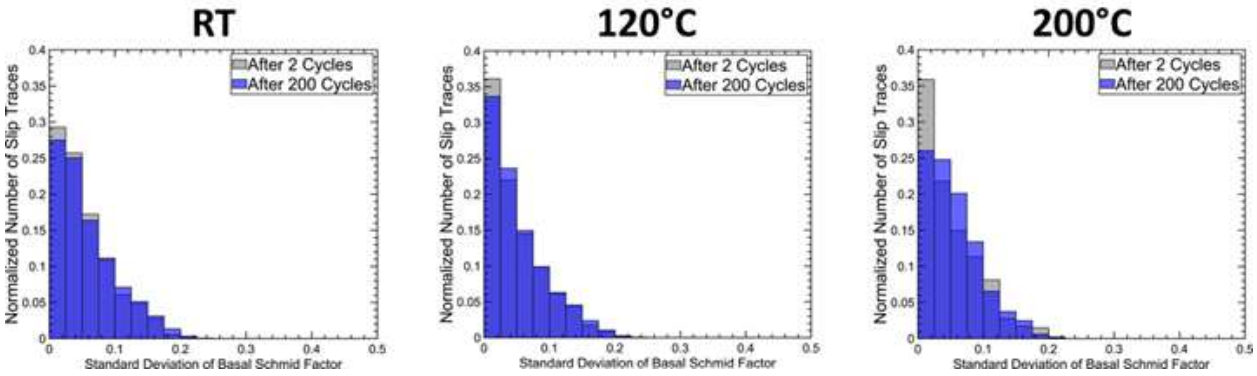

Figure 12. Standard deviation of basal Schmid factors for each slip trace at RT, 120°C, and 200°C. The individual grains that each trace traversed exhibited small variations in orientation.

At all temperatures, basal slip initiated early and dominated with cycling, making up over 55% of the total slip activity. Basal slip was expected as it is relatively easily activated, but unexpectedly, there was less than 15% prismatic slip activity. Rather, pyramidal slip was the second most active system at all temperatures and cycles. Pyramidal slip is reported as being 3-5 times more difficult to activate than basal and prismatic slip in Ti-6242 [2, 5, 40], yet in every loading case it accounted for more than 25% of slip activity, Figure 13. This is likely due to the exhaustion of easily activated basal slip, followed by the subsequent activation of slip in neighboring regions that favored pyramidal over prismatic slip; this will be further discussed in the context of the relative slip locations, active Schmid factors, and slip travel lengths. It should be noted that it was not possible to distinguish between the <c+a> vs <a> pyramidal slip from the surface traces, and these were counted together as pyramidal slip. While <c+a> pyramidal slip is known to have a CRSS 3-5 times larger than basal and prismatic slip, <a> type pyramidal slip is reported as having a CRSS ~0.9 - 1.1 times larger than basal and prismatic slip in near-alpha titanium alloys [41,42]. Therefore, it is thought that the slip activity is <a> type pyramidal slip, but this cannot be confirmed without further analysis.

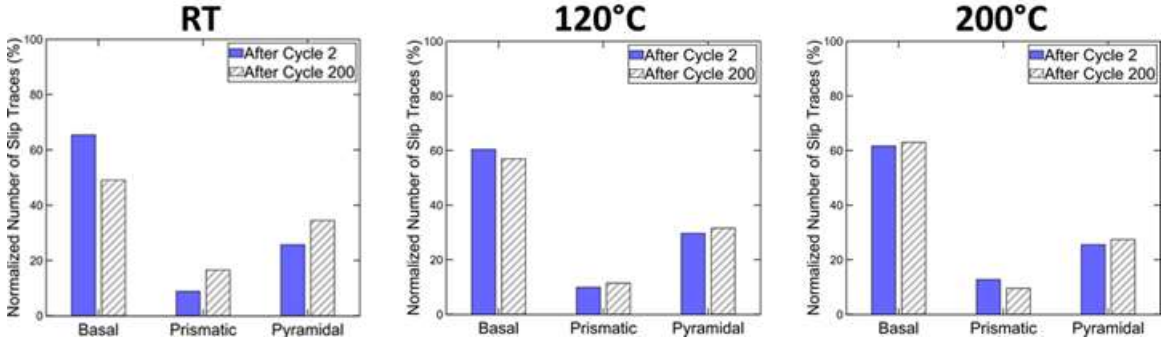

Figure 13. Active slip systems for the identified slip traces after 2 and 200 cycles at RT, 120°C, and 200°C. Basal slip initiated early and continued to dominate with cycling, but there was little long-range prismatic activity. Rather, the relatively high activity of pyramidal slip was attributed to the exhaustion of easily activated basal

slip, and the subsequent activation of slip in neighboring regions that favored pyramidal over prismatic slip.

Most basal slip traces (>60%) were longer than 80 microns, extending up to 200 microns in length at RT and beyond 1000 microns in length at 120°C and 200°C, Figure 14. Despite a larger number of pyramidal slip planes, slip traces observed on pyramidal <a> and/or <c+a> slip systems were typically significantly shorter and less numerous than basal slip traces, with the shortest pyramidal slip traces at RT. In all cases, over 80% of pyramidal slip traces traversed less than 80 microns. At RT, 100% of the observed pyramidal traces were less than 80 microns long. This may be attributed to the accommodation of internal stresses and/or load shedding, where a localized stress was imparted on a hard grain after significant deformation occurred in the nearby basally soft grains.

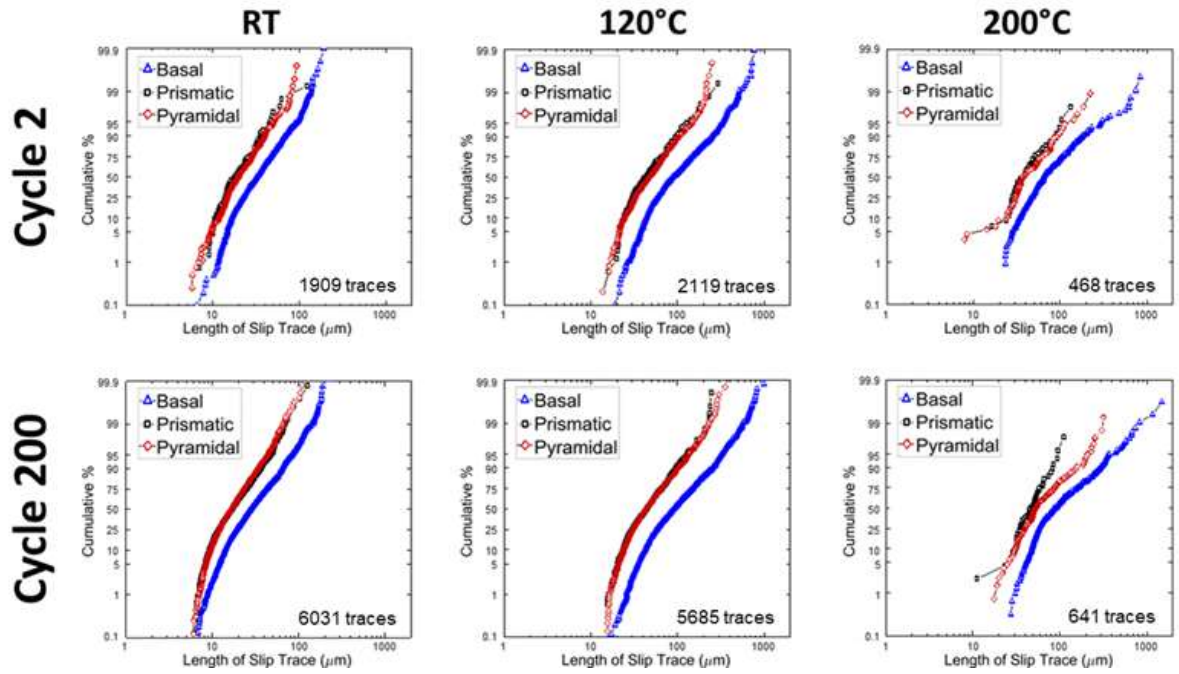

Figure 14. Cumulative distribution functions (CDFs) of slip length and family after 2 and 200 cycles at RT, 120°C, and 200°C. The bulk of deformation at all temperatures was accommodated by long-range basal slip in co-located grains, and shorter pyramidal slip in nearby grains that were not necessarily co-located.

Significant slip below the macroscopic yield strength, as in this work, has also been observed in prior experimental studies, although the identified slip trace lengths and families differ [14, 23, 41, 43-45]. Experiments on surface slip activity in Ti-6-4 have uniformly observed an onset of basal slip first, with prismatic slip then occurring at slightly higher loads [14, 23, 43, 44]. The CRSS required to activate basal and prismatic slip in near-alpha titanium alloys is close, where some work has observed a slightly lower CRSS for basal than prismatic slip [2, 5, 9, 17, 18, 40] and vice versa [23, 41, 44]. The reported CRSS required to activate each slip system varies with alloy and microstructure. In the RT *in-situ* tensile loading of Ti-6-4 at globally applied strains below 0.71%, Echlin et al. identified primarily basal slip across two or fewer grains. In contrast,

at globally applied strains of 0.71% and above, they largely observed long-range prismatic slip that traversed the entire length of the prismatic soft MTR, through as many as 20 grains. Lavogiez et al. [44] had similar findings in dwell fatigue experiments on Ti-6-4 at RT, where they observed basal slip dominating in individual soft grains during early dwell cycles at 90% of macroscopic yield. With additional cycling they observed significant prismatic slip in individual grains. They repeated the test, this time loading to a higher stress of 94% of macroscopic yield and observed the onset of prismatic slip earlier than for the 90% of yield case. Zhang et al. also experimentally observed both basal and prismatic slip activity after loading to ~3% strain in Ti-6-4, but that prismatic slip dominated [45]. In this work, even after 200 dwell cycles at a peak stress of 90% of yield, significant prismatic slip was not detected at any temperature. It is important to note that these other studies were performed on Ti-6-4, which is known to have a smaller dwell debit than Ti-6242 at room temperature. When loaded to 90% of the macroscopic yield strength at room temperature, Ti-6-4 only exhibits a dwell debit of ~2-3 times the LCF lifetime, while Ti-6242 has a dwell debit of ~10-20 times the LCF lifetime [4]. While the mechanisms behind the dwell debit are believed to be the same for both materials, one would expect there to be a difference in the strain heterogeneity and load shedding behavior relative to loading and temperature. Because of this unexpected observation, TEM studies are underway to investigate the lack of prismatic slip activity.

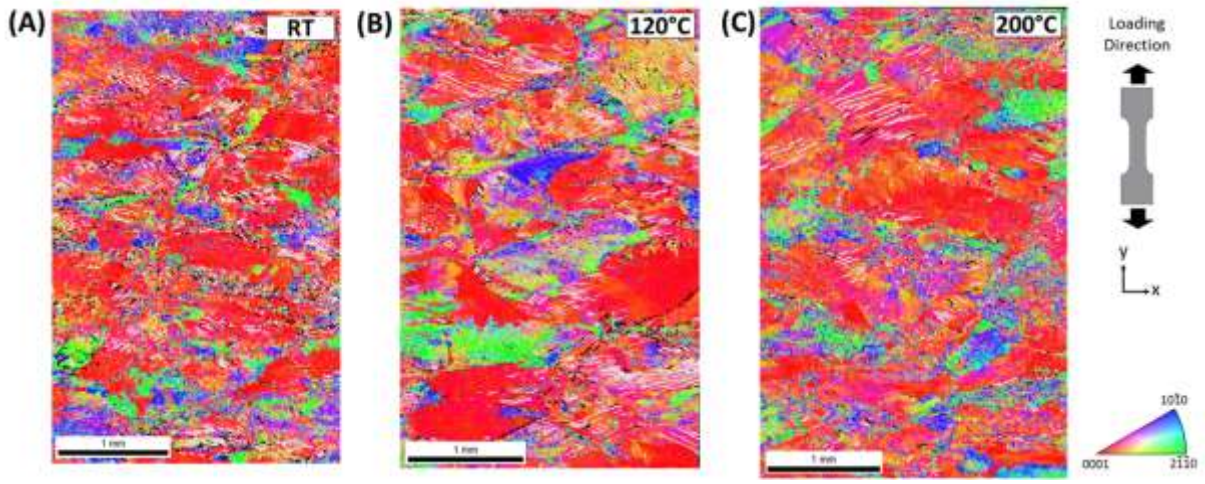

Figure 15. Basal (light gray) and pyramidal (black) slip traces overlaid on the IPF map for (A) RT, (B) 120°C, and (C) 200°C. Basal slip traces exist in basally soft grains within hard MTRs, and pyramidal slip exists in nearby grains. This is attributed to the accommodation of internal stresses after basal slip exhaustion.

While the co-location of grains was a driving factor for basal slip formation, this did not appear to be as important a factor in pyramidal slip formation. The bulk of deformation at all temperatures was accommodated by long-range basal slip in co-located grains (favorably oriented for basal slip), and shorter pyramidal slip in nearby grains that were not necessarily co-located (favorably oriented for pyramidal slip). All pyramidal slip occurred through grains with a pyramidal Schmid factor greater than 0.3, and over 70% of the pyramidal slip traces were in grains that had a pyramidal Schmid factor greater than 0.4, Figure 11. This minimum requirement on the pyramidal Schmid factor did not change with additional cycling.

After two cycles, over 99.5% of basal slip occurred in grains with a high basal Schmid factor (>0.3) at all temperatures, Figure 11. However, with additional cycling from 2 to 200 cycles, the Schmid factor required to initiate basal slip dropped significantly at both RT and 120°C (from 0.21 to 0.08 and 0.22 to 0.08, respectively). After 200 cycles at both RT and 120°, approximately 8% (7.8% and 8.2% respectively) of all basal slip was through grains with a basal Schmid factor lower than 0.25. At 200°C, no such drop in the required basal Schmid factor occurred with additional cycling (the minimum remained constant at 0.35), and 90% of all active basal slip activity had a basal Schmid factor greater than 0.4 after both 2 and 200 cycles. Prior work has observed slip primarily occurring in individual soft grains with a basal Schmid factor above 0.4. A tensile experiment observing grain level slip activity in Ti-6-4 loaded to ~3% strain by Zhang et. al and a dwell fatigue experiment on Ti-6242 by Hemery et al. both observed basal activity in grains with a high basal Schmid factor, but there was some slip activity in soft grains with a basal Schmid factor of 0.2 to 0.4 [23,45]. These studies align with the present study on MTRs, where at all temperatures most long-range plastic slip bands traversed through grains with a basal Schmid factor above 0.4, but a non-negligible number of basal slip traces occurred through grains with a lower basal Schmid factor.

The proposed mechanism for slip activity in regions with low basal Schmid factors and in less favorable hard oriented regions at RT and 120ºC is as follows. Deformation was initially and largely accommodated by basal slip in well-oriented grains, Figure 11. Prismatic and pyramidal slip was found, by visual inspection, to largely occur in grains where nearby grains were deformed heavily by basal slip, Figure 14. This basal slip could not traverse easily into the neighboring hard grain, and could therefore create dislocation pileups and associated internal stresses [46]. This internal stress and/or exhaustion of basal slip resulted in deformation either on less favorable slip systems in that grain, or in neighboring hard grains. Pilchak et al. [47] observed both of these mechanisms in TEM foils extracted from beneath dwell fatigue crack nucleation sites in Ti-8Al-1Mo-1V. In our work, these secondary slip processes occurred primarily by pyramidal slip in grains with a high pyramidal Schmid factor, but a small amount of prismatic slip also occurred. The grains that slipped pyramidally required a high Schmid factor, as pyramidal slip is more difficult to activate than prismatic slip. Those that deformed prismatically had a more random distribution of prismatic Schmid factors (with a small peak at around 0.125), based on which grain orientations were adjacent to the long-range basal slip, Figure 11 and 14. Whether the basally-soft grains must be surrounded by hard grains to exhibit long-range slip activity is a topic for further research. The moderate number of active pyramidal slip systems indicates that dwell debit and slip activity are not solely orientation dependent, and that there is the additional impact of the surrounding neighborhood. Additionally, pyramidal slip activity could indicate stress redistribution after more favorable slip systems are exhausted and a stress localization is created due to the high level of deformation in the basally soft regions [44]. This is still an open question and an active area of interest.

4.4 Implications for MTR Identification

The results of this work are relevant to the strategies one might employ when segmenting MTRs from EBSD data for use in material characterization and modeling. As mentioned earlier, prior approaches allow for a relatively large misorientation tolerance (~20°) of the proper crystallographic misorientation or the c-axis misorientation and also permit clustering of non-

contiguous groups of alpha phase into the MTR. These approaches result in MTR segmentations that compare favorably with the overall size of the faceted initiation sites of fractured dwell fatigue samples that are observed at the initiation sites of samples fractured due to dwell fatigue [7,46] and appear to adequately capture the effect of MTRs on mean material behavior [8,35,36,48]. These segmentation strategies are also appropriate for modeling studies which consider MTR-influenced crack growth behavior. [49].This is an appropriate choice because the fracture mode depends most strongly on crystallographic orientation [38] than it does on fracture mode [50]. Yet, there have been no systematic investigations with enough samples tested followed by detailed characterization to determine if these segmentation parameters adequately capture the MTRs that control the minimum, or life-limiting, behavior.

When considering the mechanisms that lead to crack initiation, however, the above criteria may not be the most accurate representation of the regions capable of developing slip bands that span many alpha grains and are therefore capable of developing strong dislocation pileups that contribute to crack nucleation. Instead, the regions of intense slip occur in subdomains of active basal-soft grains embedded within traditionally defined, slightly harder MTRs. Segmentation strategies for crack initiation need to include a requirement for grain connectivity (Figure 6) and, likely, a reduced point-to-point c-axis misorientation tolerance. The grains involved in the development of long slip bands (that form the dislocation pileup and associated stress concentration critical in load shedding and crack nucleation) also required a higher degree of alignment than the ~20° tolerance used to segment MTRs in prior studies [8, 35,36]. Furthermore, specific attention should be given to the volume fraction and size of regions capable of deforming by basal slip as these are the structural units which are developing the most intense slip bands and which act as the “soft grain” in the classic hard/soft model of dwell crack nucleation. A low volume fraction of MTRs in this orientation would correlate to improved dwell fatigue crack nucleation resistance, which is consistent with (and only a small refinement) to the work of Woodfield et al. [35]. Since MTRs are important with respect to both crack nucleation and crack propagation, they should be characterized from these two perspectives depending on the intended use of the data.

Finally, we found no evidence that MTRs well-oriented for prismatic <a> slip could develop similarly long slip bands. While seemingly contradictory with the results of [23, 43-45], who observed the activation of prismatic slip, it is worth noting that these investigators were looking at the individual crystallite scale and not the aggregate response of many crystallites. A TEM investigation of the current samples is underway to determine the extent of prismatic <a> slip in suitably-oriented grains, but the present work shows that prism <a> slip bands do not readily organize into long slip bands traversing many grains (Figure) and hence may not be suitable to act as the “soft grain” in the currently accepted dwell fatigue crack nucleation mechanism. One obvious reason for this type of behavior would be that if a single prism <a> slip system has a high resolved shear stress, there are, because of crystal symmetry, a multitude of other prism and pyramidal <a> slip systems that could operate to relieve the stress concentration associated with a pileup. In contrast, there is only one basal plane orientation per grain and if these systems are highly stressed, there is necessarily lower resolved shear stress on the easy-to-operate pyramidal and prism <a> slip systems offering fewer opportunities for cross-slip. Such an effect could be exacerbated by the presence of Ti3Al, which is known to further promote slip planarity.

5. CONCLUSIONS

An *ex-situ* study of plastic strain accumulation in Ti-6242 was conducted under dwell fatigue loading at room temperature (RT), 120°C, and 200°C to characterize slip activity and its effects on dwell fatigue lifetimes. Our findings indicate that current segmentation approaches may not be sufficient to capture the intricate details that govern whether or not a particular MTR will develop long-range slip. Rather than slip being accommodated homogeneously and diffusely throughout soft-oriented MTRs, we found that plastic slip was instead accommodated by subfeatures within classically segmented MTRs. These subfeatures were well-oriented for basal slip, with the basal slip traces of the individual alpha particles spatially aligned.

- Slip does not transmit through the entirety of traditionally-defined MTRs, but rather is driven by a contiguous group of basal-oriented grains. This differs from the behavior of MTRs in crack growth studies, where the similarly oriented grains do not need to be interconnected to behave cooperatively to permit rapid crack growth. The observed slip systems and Schmid factors in this study redefine and narrow our definition of MTRs that are damaging under dwell fatigue loading. In particular, these results suggest the necessity of grain interconnectivity and a smaller spread in c-axes should be used when identifying the boundaries of a MTR.
- There was both a greater number and a faster accumulation of slip traces at temperatures that exhibit a dwell debit in Ti-6242 (RT and 120°C) versus that which does not (200°C). The lack of slip activity at 200°C may be related to the temperature dependence of strain rate sensitivity[17,19], where a more rapid stress relaxation occurs with increasing temperature, thereby reducing the number of dislocations in a given pileup and resulting in lower effective stresses due to decreased localized plastic strain accumulation.
- At all temperatures (RT, 120°C, and 200°C), new slip traces occurred largely in regions that had already exhibited slip. There were no locations that exhibited little slip activity after two dwell cycles and subsequently accumulated significant slip. This supports the conjecture that slip and its evolution under dwell cycling are microstructurally driven by cooperative grain groupings that allow the traversal of contiguous slip activity.

- At all temperatures (RT, 120°C, and 200°C), grains that behaved cooperatively and exhibited long-range plastic slip were (i) co-located; (ii) had high basal and/or pyramidal Schmid factors, with basally-soft slip dominating; and (iii) exhibited small variations in orientation. There was little observed long-range prismatic slip activity, despite it being typically reported as the softest slip system. These observations do not necessarily imply no prismatic slip is occurring, but that if so, it does not manifest as long-range planar slip traces visible on the surface of the sample during dwell fatigue at 90% of macroscopic yield.

- Deformation at all temperatures was largely accommodated by long-range basal slip in co-located grains with high basal Schmid factors, and shorter pyramidal slip in nearby grains with high pyramidal Schmid factors. No significant prismatic or pyramidal slip was observed to occur independently in areas far from those of basal slip. This is likely due to internal stresses initiating the activation of less favorable slip in the neighboring grains following the exhaustion of basal slip, indicating that the dwell debit is not solely

orientation dependent and that we must also consider the effect of microstructural neighborhood.

- With cycling at RT and 120°C, the minimum Schmid factor required to initiate basal slip decreased from ~0.2 to ~0.08; however, at 200°C, the basal Schmid factor required to initiate basal slip remained constant at 0.35. This is due to the exhaustion of easily available slip activity while needing to accommodate additional deformation with cycling at RT and 120°C. At 200°C, little additional deformation accumulated with cycling. Between 2 to 200 dwell cycles, the number of slip traces increased by a factor of 2-3 at both RT and 120°C, but only increased by a factor of 1.4 at 200°C (Table 2).

- Pyramidal slip typically manifested in short traces. The relatively high amount of pyramidal slip was likely due to two reasons: 1) slip primarily occurred through grains with their c-axis 30-45 degrees relative to the loading direction, and which were therefore well oriented for both basal and pyramidal slip; and 2) some pyramidal slip occurred in grains with a high pyramidal Schmid factor (>0.3) that were located near basal slip activity, likely due to the internal stresses and stress redistribution caused by a significant amount of basal slip. It is important to note that due to the projections of the surface traces on the surface of the sample, it is not possible to distinguish between <a> and <c+a> pyramidal slip. While <c+a> pyramidal slip is known to have a CRSS 3-5 times larger than basal and prismatic slip in near-alpha Ti alloys, <a> type pyramidal slip is reported as having a CRSS ~1.1 times larger than basal and prismatic slip in near-alpha Ti alloys [41,42]. Therefore, it is suggested that the pyramidal slip activity is <a> type pyramidal slip, but cannot be confirmed without further investigation.

6. REFERENCES

1. Cuddihy, M. A., Stapleton, A., Williams, S., Dunne, F. P. E. (2016). *International Journal of Fatigue*, 97, 177–189.
2. Gong, J., Wilkinson, A.J. (2019). *Acta Materialia*, 57(19) 5693-5705.
3. Evans,W.J., Bache M.R. (1994). *International Journal of Fatigue*, 16 (7), 43–52.
4. Bache MR. (2003). *International Journal of Fatigue*, 25, 1079–1087.
5. Hasija, V., Ghosh, S., Mills, M.J., Joseph, D.S. (2003). *Acta Materialia*, 51, 4533-4549.
6. Qiu, J., Ma, Y., Lei, J., Liu, Y., Huang, A., Rugg, D., & Yang, R. (2014). *Metallurgical and Materials Transactions A*, 45(13), 6075–6087.
7. Sinha, V., Spowart, J. E., Mills, M. J., & Williams, J. C. (2006). *Metallurgical and Materials Transactions A*, 37(5), 1507–1518.
8. Pilchak, A. L., Tucker, J. C., & Weihing, T. J. (2017). *From Microstructure Investigations to Multiscale Modeling: Bridging the Gap*, 41–66. https://doi.org/10.1002/9781119476757.ch2
9. Venkatramani, G., Ghosh, S., & Mills, M. (2007). *Acta Materialia*, 55(11), 3971–3986.
10. Rugg, D., Dixon, M., & Dunne, F. P. E. (2007). *Journal of Strain Analysis for Engineering Design*, 42(4), 269–279.
11. Le Biavant, K., Pommier, S., & Prioul, C. (2002). *Fatigue and Fracture of Engineering Materials and Structures*, 25(6), 527–545.
12. Glavicic, M. G., Bartha, B. B., Jha, S. K., & Szczepanski, C. J. (2009). *Materials Science and Engineering A*, 513–514(C), 325–328.
13. Germain, L., Gey, N., Humbert, M., Bocher, P., & Jahazi, M. (2005). *Acta Materialia*, 53(13), 3535–3543.
14. Echlin, M.P., Stinville, J.C., Miller, V.M., Lenthe, W.C., Pollock, T.M. (2016). *Acta Materialia*, 114,164-175.
15. Lunt, D., da Fonseca, J. Q., Rugg, D., & Preuss, M. (2017). *Materials Science and Engineering A*, 680, 444–453.
16. Winstone M.R., Weaver M.J. (1984). Titanium science and technology: proceedings of the fifth International Conference on Titanium (Vol. 4.).
17. Ozturk, D., Shahba, A., Ghosh, S. (2016). *Fatigue Fracture Engineering Material Structures*, 39, 752-769.
18. Williams, J.C., Baggerly, R.G., Paton, N.E. (2002). *Metallurgical and Materials Transactions A*, 33(3), 837-850.
19. Zhang, Z., Cuddihy, M.A., Dunne, F.P. (2015). *Proceedings Royal Society A*, 471: 20150214.
20. Zheng,Z., Balint, D., Dunne,F.P.E. (2017). *Journal of the Mechanics and Physics of Solids*, 107, 185–203.
21. Jun, T.-S., Zhang, Z., Sernicola, G., Dunne, F. P. E., & Britton, T. B. (2016). Local strain rate sensitivity of single α phase within a dual-phase Ti alloy. Acta Materialia, 107, 298–309.
22. May, Katelun. Small Scale Tensile Testing of Titanium Alloys. Electronic Thesis or Dissertation. Ohio State University, 2010. *OhioLINK Electronic Theses and Dissertations Center*. 25 Apr 2020.
23. Hémery, S., Villechaise, P. (2017). *Materials Science and Engineering A*, 697, 177-183.

24. Littlewood, P. D., & Wilkinson, A. J. (2012). *International Journal of Fatigue*, 43, 111–119.
25. M.A. Sutton, N. Li, D.C. Joy, A.P. Reynolds, and X. Li. (2017). *Experimental Mechanics*, 47 775–787.
26. M.A. Sutton, N. Li, D. Garcia, and N. Cornille. (2007). *Experimental Mechanics*, 47 789–804.
27. Kammers, A. D., & Daly, S. (2011). *Measurement Science and Technology*, 22(12), 125501.
28. Lenthe, W., J.C. Stinville, M. Echlin, Z. Chen, S. Daly, and T. Pollock. (2018). *Ultramicroscopy*, 195, 93-100.
29. Chen, Z., W. Lenthe, J.C. Stinville, M. Echlin, T.M. Pollock, and S. Daly. (2018). *Experimental Mechanics*, 58(9), 1407-1421.
30. Montgomery, C. B., Koohbor, B., & Sottos, N. R. (2019). *Experimental Mechanics*, 59(7), 1063–1073.
31. Vic-2D [software]: Correlated Solutions Inc, Columbia, SC, 2009.
32. Chen, Z., S. Daly. (2018). *Materials Science and Engineering A*, 736, 61-75.
33. Chen, Z., Daly, S. H. (2017). *Experimental Mechanics*, 57(1), 115–127.
34. Bachmann, F., R. Hielscher and H. Schaeben. (2010). *Solid State Phenomena*, 160, 63–68.
35. Woodfield, A. P., Gorman, M. D., Sutliff, J. A., & Corderman, R. R. (1998). *In TMS Fall Meeting '98* (pp. 111–118).
36. Woodfield, A. P., Gorman, M. D., Sutliff, J. A., & Corderman, R. R. (1995). *In Titanium'95: Science and Technology* (pp. 111–118).
37. Pilchak, A. L., Shank, J., Tucker, J. C., Srivatsa, S., Fagin, P. N., & Semiatin, S. L. (2016). *Integrating Materials and Manufacturing Innovation*, 5(1), 259–276.
38. Pilchak, A. L., Young, A. H., & Williams, J. C. (2010). *Corrosion Science*, 52(10), 3287–3296.
39. Groeber, M.A., Jackson, M.A. (2014*). Integrating Materials*, 3, 56–72.
40. Li, H., Mason, D. E., Bieler, T. R., Boehlert, C. J., & Crimp, M. A. (2013). Acta Materialia, 61(20), 7555–7567.
41. Bridier, F., Villechaise, P, Mendez, J. (2005). *Acta Materialia*, 53, 555–567.
42. Jones, I. P., & Hutchinson, W. B. (1981). *Acta Metallurgica*, 29(6), 951–968.
43. Hémery, S., Dang, V. T., Signor, L., Villechaise, P. (2018). *Metallurgical and Materials Transactions A*, 49(6), 2048–2056.
44. Lavogiez, C., Hémery, S., & Villechaise, P. (2020). *International Journal of Fatigue*, 131, 105341.
45. Zhang, Z., Lunt, D., Abdolvand, H., Wilkinson, A. J., Preuss, M., Dunne, F. P. E. (2018). *International Journal of Plasticity*, 108, 88–106.
46. Pilchak, A. L., & Williams, J. C. (2011). Metallurgical and Materials Transactions A, 42(4), 1000–1027.
47. Pilchak, A. L., Brandes, M. C., Williams, R. E. A., & Williams, J. C. (2012). *In Ti 2011 - Proceedings of the 12th World Conference on Titanium* (Vol. 2, pp. 993–997).
48. Venkatesh, V., Tamirisa, S., Sartkulvanich, J., Calvert, K., Dempster, I., Saraf, V., … Pilchak, A. (2016). *In Proceedings of the 13th World Conference on Titanium* (Vol. VI, pp. 1907–1912).
49. Pilchak, A. L. (2014). *Scripta Materialia*, 74, 68–71.

50. Ward-Close, C. M. (1980). In Proceedings of the Fourth International Conference on Titanium (Vol. 3, pp. 1749–1175).

LIST OF SYMBOLS, ABBREVIATIONS, AND ACRONYMS

AFRL	Air Force Research Laboratory
CDF	Cumulative Distribution Functions
CPFE	Crystal Plasticity Finite Element
CRSS	Critical Resolved Shear Stress
DIC	Digital Image Correlation
EBSD	Electron Backscatter Diffraction
FOV	Field of View
IPF	Inverse Pole Figure (Map)
LCF	Life Cycle Fatigue
MTR	Microtextured Regions
PID	Proportional Integral Derivative
RT	Room Temperature
RXCM	Metals Branch, Structural Materials Division, Materials and Manufacturing Directorate of AFRL
SEM	Scanning Electron Microscopy
SNR	Signal-To-Noise Ratio
SPLCF	Sustained-Peak Low-Cycle Fatigue
TEM	Transmission Electron Microscopy